




## Oblique and parallel modes of the bistable bluff body wake

Simran Singh Panesar <sup>\*</sup>, Hao Xia , and Martin Passmore 

*Aeronautical and Automotive Engineering Department, Loughborough University,  
LE11 3TU, United Kingdom*



(Received 5 July 2022; accepted 12 July 2023; published 9 August 2023)

Turbulent bluff body flows exhibit large-scale, low frequency dynamics associated with symmetry breaking in the wake which compromise stability and increase surface pressure drag. Previous tomographic PIV had detailed that these instabilities were associated with the stochastic reorientation of a hairpin featuring a near-base “head” connected to counter-rotating streamwise “tails” extending downstream. To better understand the associated flow physics, a half-axisymmetric bluff body is assessed by means of particle image velocimetry and pressure measurements. By application of proper orthogonal decomposition (POD) and an assessment of spanwise phase difference using a Morlet wavelet analysis, we show that the asymmetry of the wake region is intrinsically linked to a large scale circulation reversal responsible for the switch to the opposing symmetry breaking state. The antiphase relationship across the base is established by propagation of an oblique wave in the cross-stream direction at separation and as a result, the wake becomes twisted and skewed to one side inducing an asymmetric base pressure gradient. The two most energetic modes in the near wake are halved with respect to rectilinear bistable bodies; the first shows a helical topology with lateral asymmetry and the second shows a symmetry preserving condition with two counter rotating vortices at each side. Across the switch, the unsteady second mode briefly characterizes the wake. The associated parallel shedding regime with reduced asymmetry promotes axial motion (bubble pumping) which is coupled to an optimal, low drag condition.

DOI: [10.1103/PhysRevFluids.8.084601](https://doi.org/10.1103/PhysRevFluids.8.084601)

### I. INTRODUCTION

Bluff body wakes feature slow global behaviors associated with symmetry breaking. Following separation from the trailing edge, a large, chaotic, recirculating bubble is formed which is instantaneously asymmetric with symmetry only being restored upon averaging for a sufficiently long time. The asymmetric wake creates a nonoptimal condition with increased base pressure drag and an induced side force. For rectilinear geometries, “bistability” (or bi-modality) develops via slow, intermittent switches between two stable reflectional symmetry breaking (RSB) states with an intermediate reflectional symmetry preserving (RSP) state across the switch [1]. This is of particular relevance to ground vehicles where it is typical to investigate a simplified body of rectangular cross section, such as the Windsor or Ahmed bodies [2]. More generally, axisymmetric bluff bodies (circular cross section) feature a multistable wake due to the random rotation of a planar shedding

---

<sup>\*</sup>s.s.panesar@lboro.ac.uk

axis, hence axisymmetry is only recovered in the statistical sense upon equal exploration of many or all the possible orientations [3].

Recent tomographic particle image velocimetry (TPIV) measurements of both the bistable, Windsor [4] and multistable, axisymmetric [5] bodies dedicated to characterizing these instabilities hinted at the presence of a universal feature of the turbulent wake. The most energetic modes from a proper orthogonal decomposition (POD) of the 3D velocity field revealed both bluff bodies shared streamwise tails extending from a hairpin in the near-wake which evolved unpredictably. Similar structures were extracted in base pressure measurements, which showed the leading spatial modes, had their energy spread across two primary periodic frequencies, namely the vortex shedding ( $St_{VS} \approx 0.2$ ) and “bubble pumping” modes ( $St_{BP} \approx 0.07$ ). The bubble pumping has been documented in multiple previous investigations [3,5–9] as a symmetry preserving oscillation associated with a slow compression and expansion of the recirculation bubble resulting in an axial pulsation relative to the model base. During the expansion phases, the vortex cores can stretch downstream promoting an increased base pressure and a concomitant drag reduction. For an axisymmetric shape, this is often extracted in the  $m = 0$  mode, where  $m$  is the azimuthal wave number. Most significantly, very low frequency, intermittent activity with no distinct frequency ( $St_{VLF}$ ) but time scales up to 100–1000 times slower than those for vortex shedding [3,10] was detailed and linked with the drift of the recirculation region from its symmetric state.

Wake asymmetries appear in flows as low as  $Re \approx 400$  [11–14] and persist in excess of  $Re > 10^6$  [10,15–25]. In a phenomenological sense, similarities to the long-time dynamics can also be found in the wake of a circular cylinder at laminar Reynolds numbers ( $Re < 400$ ). An “oblique” mode with vortices being shed inclined at an angle to the cylinder axis was reported far more often than an unstable, spanwise coherent (or “parallel”) regime [14,26,27]. As the Reynolds number was increased, vortex breakdown by means of dislocations and splitting—arising from phase mismatch at separation—formed detached wedge shaped structures with increased streamwise vorticity [28–30]. These descriptions resonate strongly with the recent findings of Pavia *et al.*, as well as descriptions of “inclined” and helical shedding behaviors allowing a  $\pi$ -phase relationship across the wakes of various other bluff bodies also at turbulent Reynolds numbers [6,9,15,31]. Interestingly, despite their geometrical differences, the parallel regime of the cylinder was only seen to be stabilized with the addition of end plates closely matching the symmetrization of the finite 3D rectilinear wake with addition of a cavity [32]. Likewise, numerical simulations of the Ahmed body wake, with synthetic jet actuation for control, showed a resymmetrization following an increase of horizontally phased shedding [33]. The same research group also demonstrated the detachment of a large hairpin following the return to an RSP condition using LES [18]. From a modeling perspective, the drift of the center of pressure for both axisymmetric [34] and rectilinear [22] bluff bodies can be well approximated by a Langevin equation with a deterministic supercritical pitchfork bifurcation perturbed by an additional stochastic noise term, further reiterating a common underlying nonlinear mechanism irrespective of the geometry.

In efforts to replicate road conditions, automotive test cases regularly feature some level of ground clearance or for more generic bluff bodies, tend to be suspended in free-stream. The result is a wake which is influenced by all approaching sides often giving rise to a closed torus on average. By contrast, studies of surface mounted cubes [35], hemispheres [36], bumps [37] and cylinders [38] share a common “half-loop” or “arch-vortex” which bends in both the streamwise and spanwise axes with their ends dissipating into the viscous floor boundary layer. Therefore, these wakes also naturally feature the streamwise legs and hairpin vortices which are understood to be closely tied to the low frequency behaviors. Furthermore, surface mounted bodies present a challenge for numerical simulations as backward facing step (BFS) and bump geometries are frequently used as validation cases due to their simplicity but inherent complexity due to resolution of the boundary layer and sufficient turbulent content in the shear layer. To the authors knowledge, aside from the mirror condition studied by Grandemange *et al.* [1], there have been few efforts with focus on bistability for grounded bodies.

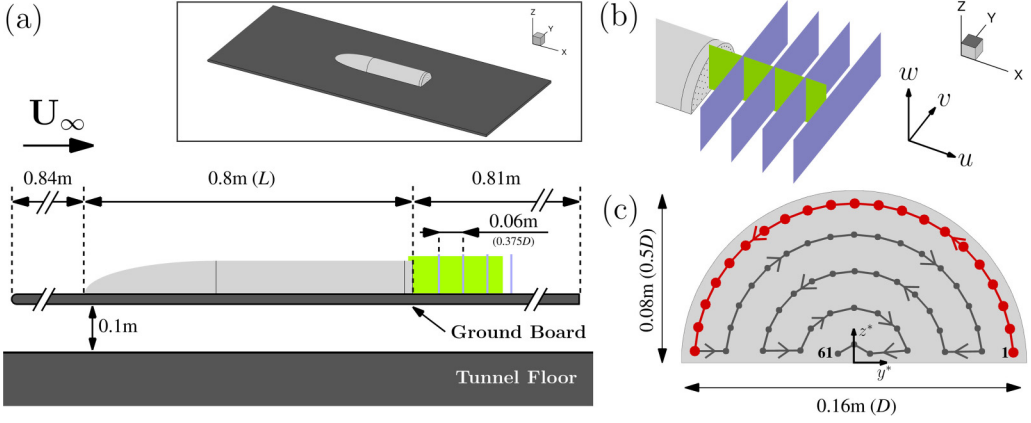


FIG. 1. Schematic of experimental procedure. (a) Model on false floor with inset showing complete setup. (b) PIV planes: Green plane depicts planar, two component at  $Y^* = 0$  and purple for stereoscopic, three component at  $X^* = 0.375, 0.75, 1.125, \text{ and } 1.5$ . 3D orientation axis and  $u, v, w$  velocity directions. (c) Model base with circles showing tap locations and cartesian coordinate system. Arrows show direction of numbering and red taps are used to deduce  $\Theta$ .

In the present work, we build on the efforts in Ref. [5] on a fully axisymmetric body but with emphasis on symmetry reduction. Despite the geometrical and Reynolds number differences, there is a strong synergy between the low Reynolds number oblique and parallel shedding modes of cylinders and the coherent structures of fully developed, turbulent finite bluff body flows. To avoid repeating previous work, we do not seek to characterize the downstream “tails” or question the validity of a near base hairpin, but rather aim to shed more light on the mechanism associated with the repositioning of this structure in the near wake. Therefore, we study a half-axisymmetric bluff body of semicircular cross section—the single symmetry plane promotes bistability and uniform curvature facilitates an azimuthally consistent vortex shedding rate. By application of POD and wavelet analysis, we show evidence of a new interpretation of the low frequency bimodal behaviours.

## II. METHODOLOGY

### A. Experimental Set Up

#### 1. Test Case

Tests were performed in the Loughborough University large wind tunnel [39] with a test section of  $W\ 1.92\text{ m} \times H\ 1.32\text{ m} \times L\ 3.5\text{ m}$  and free-stream turbulence level of 0.2%. Free-stream velocity was set to  $U_\infty = 30\text{ m/s}$  corresponding to  $Re_D = 3.2 \times 10^5$  (based on model diameter,  $D$ ) to be consistent with Pavia *et al.* [5]. The test case is derived from the same axisymmetric 2:1 elliptic nose cylinder in Ref. [5] with length  $L = 0.8\text{m}$  and diameter  $D = 0.16\text{m}$  (aspect ratio  $L/D = 5$ ), but halved to give a semicircular cross section (see Fig. 1). The bluff body was surface mounted to a ground board ( $L\ 2.45\text{ m} \times W\ 1.0\text{ m}$ ) with a curved leading edge elevated 100 mm above the wind tunnel floor to raise the model out of the thicker tunnel floor boundary layer. Distance from the leading edge of the ground board to the trailing edge of the model was 1.64 m [see inset of Fig. 1(a)] which, using turbulent boundary layer estimates, gives a displacement thickness of  $\delta^* = 0.0244D$  at separation. The current model has an aspect ratio of  $H^* = H/W = 0.5$  and zero ground clearance  $C^* = 0$  leading to a  $y^*$  instability [1]. Results are presented with the  $x, y, z$  axis and  $u, v, w$  velocities in the streamwise, spanwise, and vertical directions, respectively [see reference coordinate system in Fig. 1(b)]. All measurements with  $*$  notation have been normalized with respect to the diameter  $D$  and the freestream velocity  $U_\infty$  where necessary.

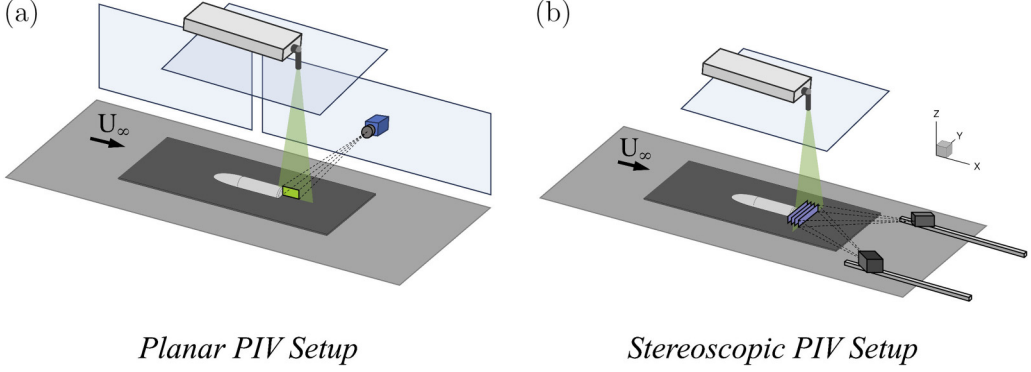


FIG. 2. Planar and stereoscopic PIV camera and laser configurations. Planar setup shows glass separating the working section and the room containing the camera. Stereoscopic setup features two boxes housing the cameras bolted to aluminium rails. In both cases, the laser is fixed to the tunnel roof and illuminates the region of interest through a glass insert.

## 2. Planar PIV

Planar 2 component PIV (2D-2C) was performed for the spanwise midplane at  $Y^* = 0$  [green plane in Fig. 1(b)]. Images were collected using a single LaVision sCMOS camera at the model height perpendicular to the plane of interest in a space outside of the tunnel with a glass window as shown in Fig. 2(a). The camera had a resolution of  $2560 \times 2160$  pixels (px) with a pixel size of  $6.5 \mu\text{m}^2$ , and was equipped with a Nikon 50 mm lens with an  $f^\#$  of 5.6. A PIVtec 45 atomizer generating DEHS droplets with a diameter of  $1 \mu\text{m}$  provided seeding from a rake located just upstream of the tunnel contraction. Particles were illuminated by a double pulsed Nd:YAG laser providing two 200 mJ, 6 ns, pulses of 532 nm wave length light mounted to the tunnel roof producing a vertical, streamwise orientated sheet after passing through a divergent sheet optic. The resulting laser sheet thickness was less than 2 mm so as to avoid erroneous in-plane motions. The laser and cameras were connected to a universal synchronizer and timing unit which ensured allowed image pairs to be acquired at a rate of 10 Hz with an interframe time of  $dt = 25 \mu\text{s}$ . This value was evaluated by performing a  $dt$  sweep in order to prevent peak locking, where the correlation peaks during processing become biased to integer pixel values [40]. Data was collected for a total of 300 seconds ( $56, 250 t^*$ ) allowing for 3000 statistically independent pairs with a field of view of  $228 \times 192$  mm, or  $11.26 \text{ px/mm}$ .

All data was processed using DaVis 10 [41]. Images were preprocessed using a sliding time average subtraction with three instances to help remove the background and distinguish the particles in the flow. Vector calculation was performed by multipass crosscorrelation with shrinking interrogation windows; the benefit of this approach is that with each pass at a specified window size, a window shift for the second frame can be iteratively refined such that fewer particles are lost between pulses facilitating a more well defined peak [42]. Two passes with an interrogation window of  $96 \times 96 \text{ px}$  with a 50% overlap were followed by four passes with a smaller window of  $16 \times 16 \text{ px}$  with a 75% overlap yielding a final vector resolution of  $1.27 \times 10^{-7} \text{ m}^2$ . Though more expensive than a square weighting and less ideal than elliptical in regions of high shear, a circular (1:1) window weighting was chosen as a compromise due to the curvature and unsteadiness of the shear layer approaching reattachment [43]. Final vector validation was evaluated using a universal outlier detection with a threshold of two [44] as well as a  $5 \times 5 \text{ px}$  median filter.

## 3. Stereoscopic PIV

Stereoscopic three component PIV (2D-3C) was performed for streamwise planes separated by a constant  $0.375D$  from the base at  $X^* = 0.375, 0.75, 1.125$ , and  $1.5$  [purple planes in Fig. 1(b)]. These locations match those used in Ref. [5] and Gentile *et al.* [23] for fully axisymmetric bodies.

Images were collected using two LaVision sCMOS cameras (see details in previous section) but with Scheimpflug adaptors to ensure focus was maintained across the plane. These were mounted to a pair of aluminium rails placed just downstream of the tunnel working section with a separation angle of  $60^\circ$  as shown in Fig. 2(b), and detailed in Ref. [45]. The laser was fixed to the roof and created a spanwise orientated laser sheet of thickness less than 2 mm. Due to the lower sampling rate of 8 Hz, the interframe time was adjusted to  $dt = 30 \mu\text{s}$ . Data was collected for a total of 300 seconds ( $56, 250 t^*$ ) matching that for the planar data, providing 2400 statistically independent image pairs with a field of view of  $400 \times 315 \text{ mm}$  ( $\pm 5 \text{ mm}$ ) or  $7.23 \text{ px/mm}$  for each location. The reduced sample size was necessary to maintain the same sampling duration with double the number of images due to RAM limitations on the acquisition PC (for convergence analysis, see the Appendix).

Vector calculation was performed with the same steps as the planar PIV, however, a geometric mask was used in the preprocessing to remove regions of no interest such as the freestream well above the model and adjusted for each camera such that the overlapped region would span  $Y^* = \pm 0.7D$ . The circular window weighting function was applied in the multipass procedure to complement the curvature of the geometry [43]. The final vector resolution was  $3.05 \times 10^{-7} \text{ m}^2$ .

#### 4. Base Pressure Measurements

Base surface pressures were measured simultaneously with a differential pressure scanner at 260 Hz from 61 pressure taps located at  $r/D = 0.053, 0.159, 0.266, 0.372$ , and  $0.463$  [see Fig. 1(c)]. In addition to the five recordings in parallel with the PIV, five additional acquisitions were performed all with yaw angle at zero for an ensemble of 3000 seconds ( $562, 500 t^*$ ).

#### B. Mathematical Formulation

After subtracting the time average, POD was applied to the fluctuating fields to extract coherent, repeating structures. For PIV, POD was only applied to the stereoscopic data at  $X^* = 0.375$  to focus attention on the plane closest to the base, and continuity is satisfied since these are three-component velocity vectors. When applied to the fluctuating components of base pressure, a cartesian coordinate system ( $y^*, z^*$ ) is used—see Fig. 1(c). The respective fields are decomposed as

$$\mathbf{F}(x, t) = \bar{\mathbf{F}}(x) + \mathbf{f}'(x, t) = \bar{\mathbf{F}}(x) + \sum_{n=1}^N \Phi_n(x) a_n(t), \quad (1)$$

where  $\bar{\mathbf{F}}(x)$  denotes the time-averaged contribution and  $\mathbf{f}'(x, t)$  the time varying turbulent fluctuation. Coherent turbulent structures are given by the optimal basis functions,  $\Phi_n(x)$  which are the “POD modes,” and their evolution by temporal coefficients  $a_n(t)$ . The number of modes,  $N$ , is dependent on the method applied: “snapshot” for PIV and “direct” for base pressures [46,47].

To be consistent with previous work [25,48], the long-time dynamics are tracked via the centroid of base pressure (subscript *CoP*) by

$$\begin{pmatrix} y_{CoP}^*(t) \\ z_{CoP}^*(t) \end{pmatrix} = \begin{pmatrix} \frac{\int y^* C_p(x, t) dx}{\int C_p(x, t) dx} \\ \frac{\int z^* C_p(x, t) dx}{\int C_p(x, t) dx} \end{pmatrix}, \quad (2)$$

where  $C_p$  is the base pressure coefficient. The barycenter of momentum deficit (subscript *CoM*) is also presented replacing  $C_p$  in Eq. (2) with the streamwise velocity loss,  $(1 - u^*)$ .

The spectral content of base pressure fluctuations is assessed by two methods to overcome the nonstationary nature of the bistability. Welch’s method [49] provides a short time Fourier transform (STFT) procedure for spectral density estimates; this is implemented with a window size of  $3750 t^*$  (20 seconds) and 50% overlap. In addition, we apply the continuous wavelet transform (CWT) to provide increased temporal resolution [50,51]. We begin by defining the analytic “Morlet wavelet function”,  $\psi_0$ , as

$$\psi_0 = \pi^{-1/4} e^{i\omega_0 \eta} e^{-\eta^2/2}, \quad (3)$$

where  $\eta$  is a nondimensional “time” parameter and  $\omega_0$  is a nondimensional frequency, here taken to be six to satisfy the admissibility condition [52]. The resulting impulse takes the form of a Gaussian weighted harmonic. Given a real valued signal,  $f(t)$ , the CWT is given by the convolution,

$$W_\psi(f)(a, b) = \langle f, \psi_{a,b} \rangle = \int_{-\infty}^{\infty} f(t) \psi_{a,b}^*(t) dt, \quad (4)$$

where  $\psi_{a,b}^*(t)$  is the complex conjugate of the modified mother wavelet as defined in (3):

$$\psi_{a,b}(t) = \frac{1}{\sqrt{a}} \psi_0\left(\frac{t-b}{a}\right), \quad (5)$$

with  $a$  and  $b$  as the scaling and translation parameters, respectively. The resulting amplitude depicts how well the signal is correlated to the modified analytic wavelet at a given instance. To compensate for smearing effects produced by the filtering procedure, wavelet synchrosqueezing [53] reassigns the activity to the peak frequency at the point in time revealing the instantaneous frequency. This was implemented using the “wsst” function within MATLAB. Wavelet power is obtained by summation of the complex amplitudes in time.

Phase differences between the red pressures taps on the model base [see Fig. 1(c)] are evaluated at both the vortex shedding and bubble pumping Strouhal numbers of  $St_{VS} = 0.2$  and  $St_{BP} = 0.065$  (i.e. one with two, two with three, and so on) giving a total of 20 pairs for pressure taps 1 to 21. This restricts attention to those closest to separation. The magnitude squared wavelet coherence ( $\rho_\psi$ ) between two adjacent pressure taps  $j$  and  $k$  is deduced,

$$\rho_\psi(j, k) = \frac{|W_{\psi,j}(a, b) W_{\psi,k}(a, b)|^2}{|W_{\psi,j}(a, b)|^2 \cdot |W_{\psi,k}(a, b)|^2}. \quad (6)$$

The complex result provides the phase angle,  $\theta$ , as

$$\theta = \arctan \frac{\text{Im}[\rho_\psi(j, k)]}{\text{Re}[\rho_\psi(j, k)]}. \quad (7)$$

The angle  $\theta$  can be used to assess propagation direction between successive taps. In this work, we focus on the net phase difference by summation of the aforementioned phase angle to give

$$\Theta = \frac{\sum_{i=1}^z \theta_i}{\pi}, \quad (8)$$

where  $i$  denotes the respective pair and  $z$  is 20 to limit attention to the red taps only. For clarity, we apply a moving average of 0.25 seconds ( $46.875 t^*$ ) to variables denoted as  $\langle [\ ] \rangle_{0.25}$ . This value is chosen to filter out the flapping and pumping modes but retain the very low frequency global instability [10].

### III. RESULTS

#### A. Time Averaged Fields

Time-averaged results are presented to demonstrate agreement with previous bluff body studies. The mean base pressure distribution depicted on the model base in Fig. 3(a) is consistent with those of fully axisymmetric shapes [3,5,23] with a favorable pressure gradient developing radially from the center toward the edges. Time-averaged pressure drag integrated over the base is obtained as  $C_{d_{b\text{mean}}} = 0.164$  which is lower than 0.189 for the full axisymmetric body [5]. It is understood that base pressure drag reduces with increased fore-body drag for axisymmetric shapes [54]. Therefore, we associate the lower value to the thicker, turbulent boundary layer at separation induced by the ground board. The contours highlight regions of reduced suction either side of the symmetry plane at  $\pi/4$  and  $3\pi/4$ , and an intermediate region at the midbase with increased suction.

Most explicitly, the spanwise planes in Fig. 3(a) show a progressive reduction in the size of the recirculation region and a thickening of the shear layer at each successive streamwise location until



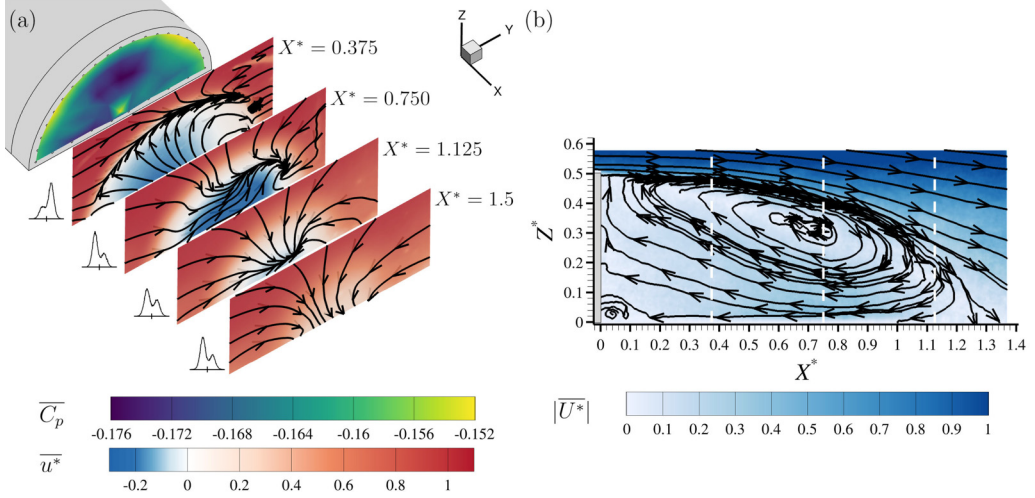


FIG. 3. (a) Time-averaged base pressure and spanwise PIV results colored by normalized time-averaged streamwise velocity with contour centered at  $\overline{u^*} = 0$  overlaid with in-plane streamlines. Histograms of  $y_{CoP}^*$  from respective pressure samples shown next to each plane. (b) Time-averaged  $Y^* = 0$  result colored by magnitude,  $|\overline{U^*}|$ , secondary vortex located at  $(0.04, 0.02)$ .

reattachment occurs at  $X^* = 1.25$  [defined from Fig. 3(b)] placing the final spanwise plane at  $X^* = 1.5$  after mean wake reattachment. This is in good agreement with wake closure of  $X^* = 1.2 - 1.3$  in Ref. [5], and Gentile *et al.* [55] who found a reattachment length of  $X^* = 1.2$  with the smallest base extension of  $d/D = 0.2$  on a similar axisymmetric body. In-plane streamlines demonstrate how the recirculating flow is drawn up at  $X^* = 0.375$  and deflected down at  $X^* = 1.125$  in agreement with the line profiles for the vertical velocity  $w^*$  at  $Y^* = 0$  in Fig. 4. The associated histograms shown next to each plane of Fig. 3(a) show that the average field is largely influenced by the bistability as all samples were taken with zero yaw. The  $X^* = 0.375$  plane shows a right side bias resulting in increased reversed flow on the left which can give reason to the disagreement in streamwise velocity between the planar and stereoscopic measurements in Fig. 4 at  $X^* = 0.375$ . It is interesting to note that the differences are less pronounced moving downstream suggesting a stronger influence of the bistability nearbase.

Figures 3(b) and 4 show the similarity to a backward facing step, with a large recirculation region aft of the bluff body and entrained flow above [35]. The blunt base clearly defines the separation point and forms a strong shear layer with minimal influence from leading edge separation due to the elliptic nose as is often the case for a surface mounted cube [56]. The intermediate plane at  $X^* = 0.75$  is shown to be in a high shear region with both the peak minimum ( $Z^* = 0.35$ ) and maximum ( $Z^* = 0.05$ ) velocity magnitude. With reference to Fig. 4, it is within this region that  $u^*$  is seen to reverse, and  $w^*$  develops a more pronounced gradient. As a result, it is likely that the near-base spanwise structures developing in the shear layer are being reorientated to form the hairpin legs. This location also coincides with the peak Reynolds stress for blunt-based axisymmetric bodies [5]. In-plane streamlines at this position show an asymmetric bias to the right; the clustering of streamlines in the shear layer is expected to be from one of the streamwise “tails” or arch vortex “legs” extending through this plane. An axial movement of the reattachment point consistent with “bubble pumping” is expected between these last two planes.

It is important to differentiate that the primary structure in the current wake is one of an inclined arch-vortex or half-loop with the ends dissipating into the viscous boundary layer in the wake (see the Appendix, Figs. 8(a), 8(c), and 8(e) for regions of high turbulence intensity which outline this structure). As this structure is convected downstream, it bends and emerges as the stretched primary

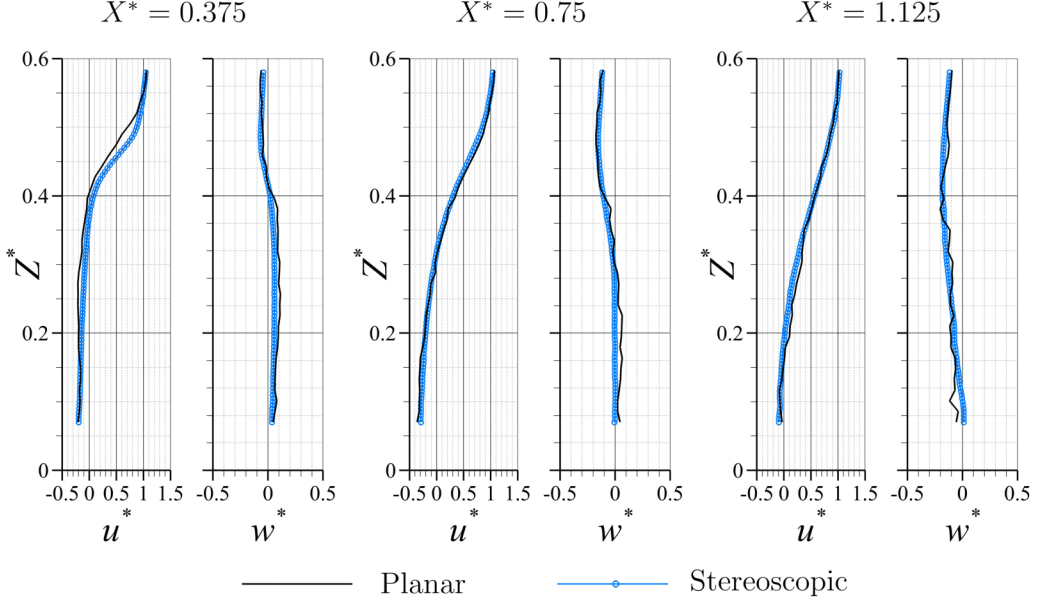


FIG. 4. Line profiles of  $u^*$  and  $w^*$  velocity at the symmetry plane,  $Y^* = 0$ . All planes are shown from  $Z^* = 0.06D$  to show consistent segments for all planes and setups.

vortex at (0.70, 0.35) in the time average at  $Y^* = 0$  in contrast with the typical closed torus found for axisymmetric geometries. Much like other surface mounted geometries, such as cubes [35], hemispheres [36], and cylinders [38], the circulation at the bottom corner (0.04, 0.02) of Fig. 3(b) is an isolated secondary vortex which forms as a result of recirculating flow impinging at the junction between the base and the ground plane. This is corroborated by the high pressure region at the lower midbase.

## B. Time Varying Fields

### 1. Velocity Field Decomposition

From a single 300 second test run, the sum of the turbulent kinetic energy of the first 10 POD modes from the PIV at  $X^* = 0.375$  is only 29% [see blue bars of Fig. 6(a)]. The low energy of the leading modes is due to the velocity vectors representing a single 2D plane within a 3D wake containing cascading scales which are not sufficiently resolved as a result of spatial averaging. Also, the fluctuation energy is being spread over a larger number of spatial modes—2400 for PIV and 61 for base pressure. The upper row of Fig. 5 depicts the two greatest contributors to the turbulent kinetic energy.

The first mode ( $\Phi_1 \cdot U \sim 15.3\%$ ) in Fig. 5(a) is associated with a lateral motion across the near-wake. The contours show a spanwise asymmetry of streamwise velocity and in-plane streamlines depict a spiral stirring. This leading, antisymmetric (RSB) mode mimics half of the lateral symmetry breaking behavior found for bistable geometries [16,57] and the  $m = 1$  mode of the axisymmetric wake. We believe this difference is a consequence of no orthogonal symmetry plane intersections, as is the case for a rectilinear or circular shape. Due to the low acquisition frequency, this dominant mode captures the long-time global dynamics as confirmed by bimodal behavior being present in its mode coefficient,  $a_1(t)$  [see Fig. 6(c) for a sample time period].

The second most energetic mode ( $\Phi_2 \cdot U^* \sim 3.1\%$ ) in Fig. 5(b) shows a more symmetric shape with strong through plane fluctuation at midbase. This RSP mode is weaker as a consequence of lateral symmetry being an unstable transient state leading to fewer realizations across the sampling period. In-plane streamlines reveal two counter-rotating vortices at each side with a cosine



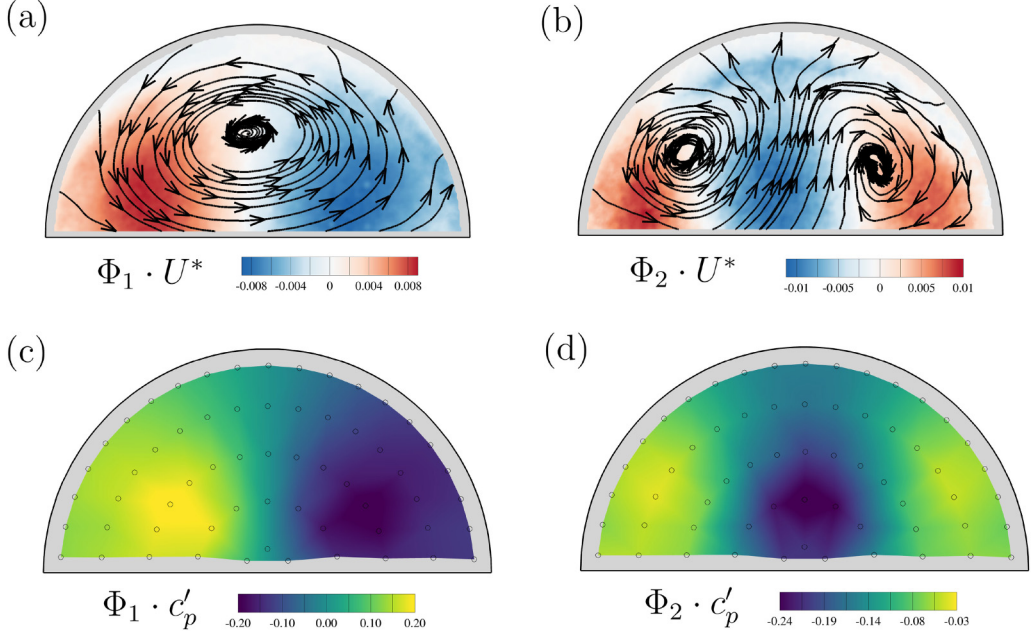


FIG. 5. POD mode shapes. Top row (a), (b) shows PIV POD mode shapes coloured by through-plane component (blue into page, red out of page) and overlaid with in-plane streamlines. Bottom row (c), (d) shows base  $C_p$  mode shapes with yellow and blue depicting positive and negative fluctuations, respectively.

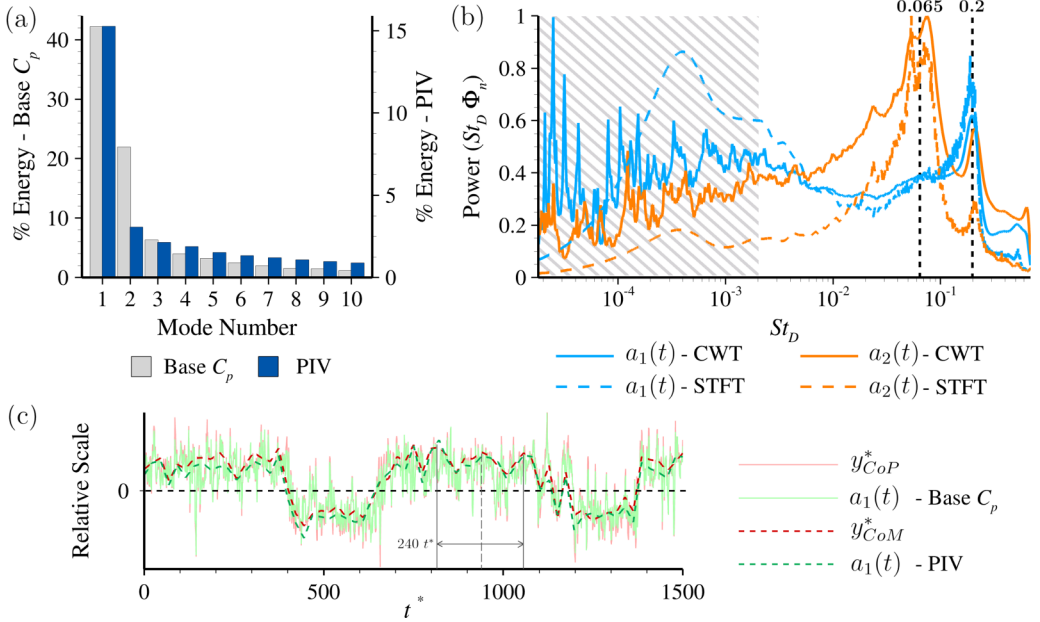


FIG. 6. Fluctuating components of velocity and pressure measurements. (a) Energy contribution from first 10 POD modes; (b) CWT (solid) and STFT (dashed) of  $a_1(t)$  and  $a_2(t)$  from base pressure data (blue: mode 1, orange: mode 2). Hashed region highlights global instability range from  $St_{VS}/100$  [10]; (c) Symmetry indicators and  $a_1(t)$  for an arbitrary switch event. Sign of  $y_{CoM}^*$  has been inverted for clarity. Peak to peak evaluation of low frequency precession shown for two periods.

distribution of the streamwise component. Again, this mode mimics half of the equivalent lateral symmetry preserving mode for rectilinear geometries [4] and the axisymmetric  $m = 0$  mode [5]. Through-plane contours invert with sign changes of  $a_2(t)$ , suggesting an axial motion of the wake characteristic of “bubble pumping” [6]. The overall topology is also consistent with the initial steady symmetric bifurcation state at low Reynolds numbers with streamwise strands [11,12].

## 2. Pressure Field Decomposition

The first two base pressure POD modes capture 64% of the fluctuating pressure field:  $\Phi_1 \cdot c'_p \sim 42\%$  and  $\Phi_2 \cdot c'_p \sim 22\%$  [see gray bars in Fig. 6(a)]. The disparity in captured content between the two datasets is given by a complete scalar field being compared to three component vectors. The higher energy of the second mode compared to the PIV is ascribed to the sampling rate of the pressure data capturing more realizations of both the slow, transient symmetric state and faster, periodic bubble pumping activity. Therefore, the energies of both are assigned to the same symmetry preserving spatial mode. This is confirmed by adopting a similar technique to Pavia *et al.* [5] to high pass filter the data which causes the order of the first two modes to swap. Nevertheless, the qualitative agreement in mode shapes is obvious [Figs. 5(c) and 5(d)].

The maximum resolvable frequencies are 130 Hz and 4 Hz for the pressure and PIV, respectively, hence the spectral analysis in Fig. 6(b) is only presented for the base pressures. Periodic contents of the two leading POD mode coefficients are well captured by both the STFT (dashed lines) and CWT (solid lines) with  $a_1(t)$  clearly showing a peak centered at  $St = 0.2$ , and  $a_2(t)$  at  $St = 0.065$ ; both these values are in excellent agreement with the quoted vortex shedding ( $St_{VS}$ ) and bubble pumping ( $St_{BP} \approx St_{VS}/3$ ) values, respectively. We also note the small peak in  $a_2(t)$  at  $St = 0.21$ , suggesting a slight amplification of the  $St_{VS}$  activity with a symmetric wake [20,26]. Most significantly, the STFT suggests broadband activity across the very low frequency range for both modes [hashed region of Fig. 6(b)] due to spectral leakage, whereas the sharp peaks of the CWT clarifies these are many rare, long wavelength, burst events.

To show the agreement in the temporal coefficients, Fig. 6(c) takes a  $1500 t^*$  segment from the test sample for the stereoscopic  $X^* = 0.375$  data and the pressure data sampled at the same time. Both datasets are nondimensionalized according to  $(1/f_s) \times U_\infty/D$ , where  $f_s$  is the respective sampling frequency. Since these are not divisible to an integer value ( $260/8 = 32.5$ ), all are presented at their full sampling rates and hence pressure derived results yield much noisier signals due to the vortex shedding. In addition to the bimodal switching, some low frequency periodicity can be identified between 700 and  $1100 t^*$  which, using a peak-to-peak method, equates to 1.56 Hz ( $St \approx 0.008$ ). The source is not entirely clear as there are no distinct features in the  $\mathcal{O}(10^{-2})$  range of Fig. 6(b) for the pressures, and so it is likely better captured by a less energetic mode. It is possible that the associated behavior is a low frequency precession of the wake whilst in an asymmetric condition as found for the axisymmetric wake [58]. The center of pressure ( $y_{CoP}^*$ ), center of momentum deficit ( $y_{CoM}^*$ —sign inverted), as well as the first POD mode temporal coefficients from each respective POD all show strong agreement suggesting that the most energetic motions of both datasets stem from the bimodality which extends the entire near wake up to  $X^* = 0.375$ . The agreement decreases significantly for subsequent spanwise planes (not shown here) likely as a result of the nonlinear shear layer expansion approaching reattachment.

Figure 7(a) focuses on an  $11\,250 t^*$  (60 second) sample from the  $X^* = 0.375$  test run. The red line and corresponding moving average shows the  $y$  coordinate of the center of pressure,  $y_{CoP}^*$ , which is used as the symmetry indicator. Across the ensemble, the symmetry plane is crossed at 1463 instances, producing an average time between bifurcations of  $384 t^*$  ( $\sim 2$  seconds), or  $St_{VLF} = 0.0026 \approx St_{VS}/77$ . The higher value obtained presently can be ascribed to the turbulent boundary layer providing additional unsteadiness to the developing shear layer, amplifying the instability [59]; however, much slower switches can be seen in Fig. 7(a) such as the interval between 7250 and  $10\,000 t^*$  ( $\sim 15$  seconds), reiterating the stochastic nature. Additionally, for geometries with more than one symmetry plane or cross-sectional aspect ratio other than one, more than one shedding rate

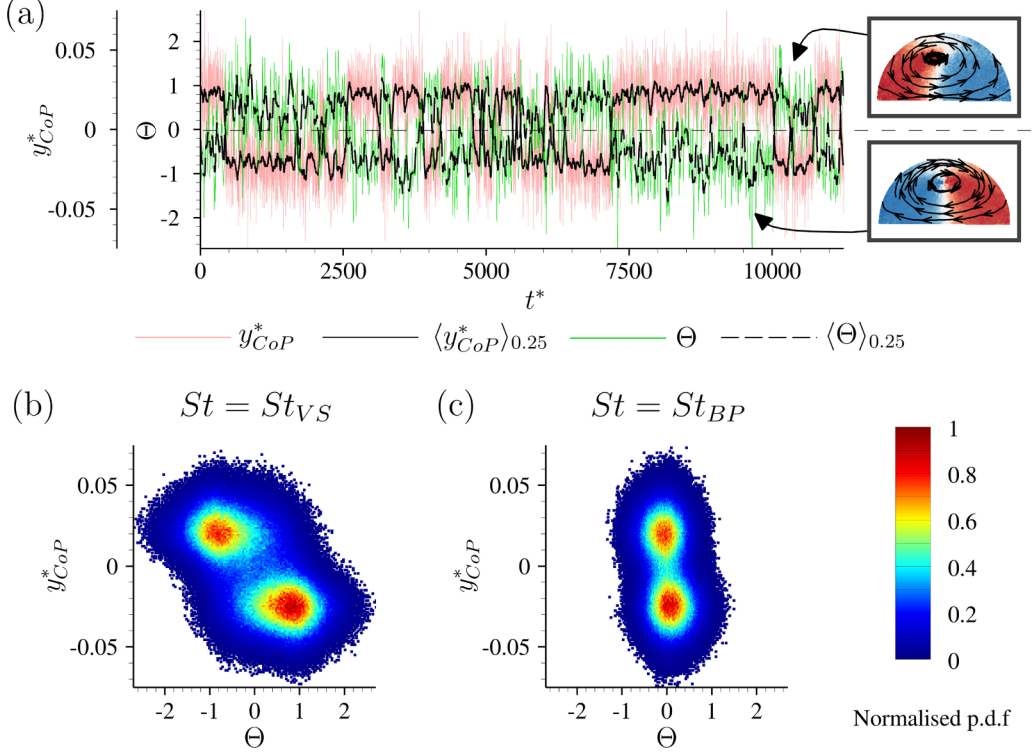


FIG. 7. Bistability and spanwise phase difference. (a) Sample interval for  $y_{CoP}^*$  and  $\Theta$  at  $St_{VS}$  with conditional POD of PIV data for each state. The second row shows joint probability density functions between the symmetry indicator,  $y_{CoP}^*$ , and (b)  $\Theta$  at  $St_{VS}$  and (c)  $\Theta$  at  $St_{BP}$ , respectively. Both are for the full 562 500  $t^*$  ensemble.

is observed [15,51,60] which gives reason to the longer settling times in each symmetry breaking state compared to the present case.

To investigate the connection to oblique shedding, the green line and associated moving average in Fig. 7(a) presents the net phase difference ( $\Theta$ ) at the vortex shedding frequency  $St_{VS}$  as described in Eq. (8). Clearly, there is a strong link between the two presented signals with both sharing the same bimodal fluctuations. At the instances of a bifurcation to the alternate RSB state, we note the shift to an opposing net phase difference indicating the taps are now being successively passed in the opposite direction: clockwise (phase lag)  $\leftrightarrow$  counterclockwise (phase lead).

To shed light on the associated dynamics in the flow field, we include conditional POD applied to the velocity vectors by binning the data into left and right RSB states according to the RMS of the normalized  $a_1(t)$ . This results in 573 (24%) and 1501 (63%) snapshots for the left and right states, respectively, which is to be expected given the asymmetry seen in Fig. 3(a). Referring to the Appendix, Fig. 8(b), both sample sizes are sufficient to provide accuracy within 0.1 m/s error. However, the extracted structure for the right state [ $y_{CoP}^* > 0$ , lower vector field in Fig. 7(a)] shows better convergence with reduced lateral asymmetry. Nonetheless, the resulting velocity vectors demonstrate that the large scale circulation reverses and the lateral asymmetry is reflected following a bifurcation.

From the joint probability density function (JPDF) in Fig. 7(b) of the full 562 500  $t^*$  ensemble, the barycenters of two attractors either side of the single symmetry plane at  $y^* < \pm 0.05$  are clearly evident [3,5,21]. Along the  $x$  axis, the data show a statistical preference to  $\Theta = \pm 1.0$  in each RSB state reiterating an antiphase relationship across the base. From this plot, it is noted that there are

a number of instances with increased phase mismatch ( $\Theta > 1.0$ ) aligning with the explanations of different shedding regimes existing concurrently for the circular cylinder [28].

When evaluating  $\Theta$  at the bubble pumping frequency,  $St_{BP}$  [see Fig. 7(c)], the attractors shift toward zero with almost all instances showing  $\Theta < 1.0$  irrespective of the degree of wake asymmetry. This result confirms that the bubble pumping is indeed base symmetric. The spanwise phase collapses from a twin-peak distribution to single, suggesting the activity at this lower frequency is the symmetric counterpart to the antisymmetric vortex shedding.

#### IV. DISCUSSION AND CONCLUDING REMARKS

To develop on the results by Pavia *et al.* for the axisymmetric and square-back bluff bodies, we have studied a test case with particular focus on symmetry reduction. Previous results had shown that a time averaged torus was formed by reorientation of a hairpin vortex with a distinct “head” close to the base connected to two counter rotating “tails” extending toward wake closure. Present 2D measurements find the halfaxisymmetric differs in forming a strongly deformed, inclined hairpin (arch) vortex with its legs dissipating into the thick, viscous boundary layer of the ground plane. The leading modes of the POD are halved with respect to those found previously, but still retain many of the same topological features. The center of pressure verified a bistable wake with switches across the symmetry plane and a preference to asymmetric states with a less explored, intermediate symmetry preserving condition. Application of the wavelet transform to supersede the traditional Fourier based approach increased spectral resolution in the very low frequency ( $St_{VLF}$ ) range and revealed sharp peaks emphasizing an intermittent “bursting” event which helps to restore a wake symmetrization [5,18].

In accordance with multiple previous investigations, an antiphase relationship ( $\Theta = \pm 1.0$ ) is found at the vortex shedding frequency ( $St_{VS} = 0.2$ ) across the base. The wavelet reveals that this asymmetry is intrinsically linked to the leading symmetry breaking mode in the near wake from a POD decomposition. The associated coherent structure is laterally asymmetric resembling a spirallike behavior in which the large scale circulation is seen to reverse in accordance with a switch to the opposing symmetry breaking state. It can be inferred from these results that in the natural, unforced bluff body wake, a successive, oblique, detachment in the cross-stream direction facilitates the lateral asymmetry of the bulk recirculating flow. It is important to note that vortex shedding actually occurs further downstream ( $X^* > 0.75$  in the present case) and is not necessarily helical itself. Rather, spanwise longitudinal rollers within the mixing layer approaching this region are believed to be inclined relative to the base enabling the “head” to settle on the lagging side and strengthen the hairpin leg on the opposite side downstream. High frequency 3D measurements or eddy resolving simulations would be required to confirm these conjectures. These could also shed more light on the low frequency motion on the order of  $St = \mathcal{O}(10^{-2})$ , identified from the temporal coefficients which is thought to be a precession or “rocking” of the hairpin head when settled in an RSB state.

Further assessment of a spanwise phase at  $St_{BP} = 0.065$  confirms a slower, base symmetric (or parallel) fluctuation which aligns with the descriptions of an axial pulsation of the wake bubble. The results suggest that the “bubble pumping” is largely invariant to the asymmetries with  $\Theta = 0$  consistently. At instances where  $\Theta \rightarrow 0$  for  $St_{VS}$ , and  $y_{CoP}^* \rightarrow 0$ , an RSP state mirroring Fig. 5(b) likely takes over with both clockwise and counterclockwise propagation existing concurrently on either side which cancel to give zero net phase difference. The bubble pumping activity is also expected to be most active during these phases due to increased streamwise vorticity enabling the recirculation bubble to stretch downstream and provide the greatest drag benefit. Coincidentally, a maximum base pressure drag reduction of  $\Delta C_{d_b} = -3\%$  [5,16,32,61] was found compared to time-averaged results at instances with near-zero  $y_{CoP}^*$ , confirming there is indeed an optimal drag state in the absence of asymmetries.

However, the relationship is far from trivial as isolating instances with  $\Theta \approx 0$  at  $St_{VS}$  does not always recover a low drag condition; it is believed that there is a time delay following the restoration of parallel regime before a drag reduction can be realized. Support is given by studies

with perimetric base blowing, such as in Ref. [62], which directly suppress asymmetry in the shear layer helping to stabilize the RSP state. In certain cases, these changes can permanently displace the formation region and provide a base pressure recovery.

### ACKNOWLEDGMENTS

The authors would like to thank Dr. Jeff Howell for fruitful discussions and valuable comments, as well as Dr. Max Varney for assistance in PIV and pressure data acquisition. Funding for this project was provided by Loughborough University.

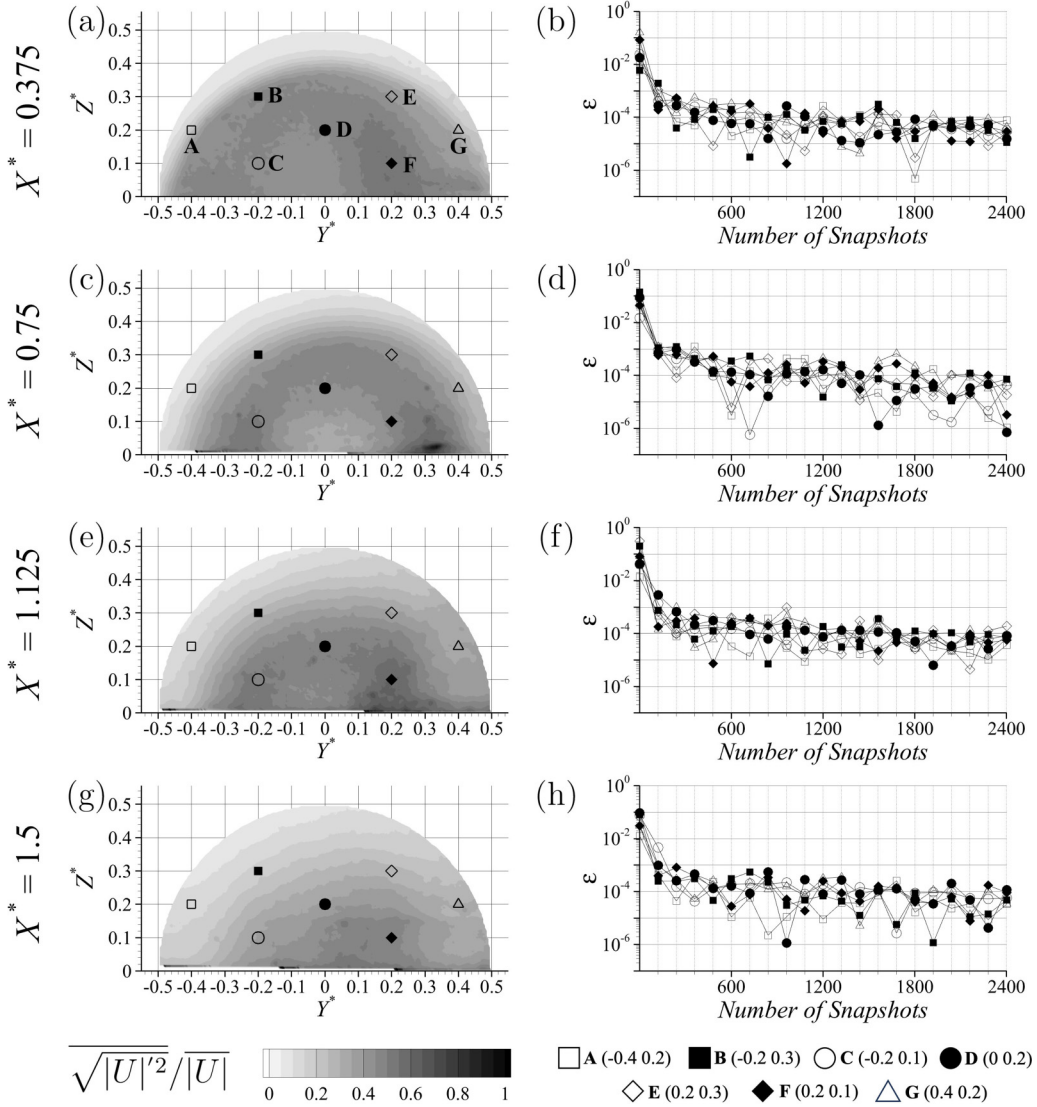


FIG. 8. Convergence of velocity field measurements. (a), (c), (e), (g), Contours of the turbulence intensity calculated with the velocity magnitude. (b), (d), (f), (h), Data from probe points A–G are assessed with respect to the normalized difference in velocity magnitude with increasing number of snapshots. Each point is separated by 120 snapshots for clarity.



## APPENDIX: VELOCITY FIELD CONVERGENCE

Given the low temporal resolution of the stereoscopic PIV at 8 Hz, the results have first been assessed for convergence to ensure that the modes extracted from the POD analysis are unaffected by the sampling time. Figures 8(a), 8(c), 8(e), and 8(g) show contours of the turbulence intensity calculated with the velocity magnitude so as to unify all three components to a single scalar. It is important to note that these values are relative to the local mean, not the freestream velocity. In the statistics community, this is analogous to the coefficient of variation. Hence, the outer regions are largely quiescent due to small variations but in the turbulent wake, the fluctuations are up to 50% of the local mean velocity magnitude. To assess the convergence of the stereoscopic measurements in more detail, seven identical probe locations are chosen for consistency and assessed for the deviation in the time averaged velocity magnitude with respect to the sample size. The normalized residual error ( $\varepsilon$ ) is calculated by

$$\varepsilon = \frac{||U|(n) - |U|(n-1)|}{U_\infty}, \quad (\text{A1})$$

where  $n$  is the number of snapshots. For clarity, Figs. 8(b), 8(d), 8(f), 8(h) present the error when increasing the sample size by 120 snapshots (15 seconds) to the maximum of 2400 (300 seconds). Irrespective of the location, the residuals show exponential decrease in error with all streamwise planes falling well below  $10^{-3}$  which corresponds to an absolute error of 0.1 m/s (0.3% of  $U_\infty$ ) within the first 600 snapshots. From 2000 snapshots and above, the change in error shows little variation asymptoting to  $10^{-4}$  (0.01 m/s, 0.03% of  $U_\infty$ ), suggesting the results are suitably converged.

- 
- [1] M. Grandemange, M. Gohlke, and O. Cadot, Bi-stability in the turbulent wake past parallelepiped bodies with various aspect ratios and wall effects, *Phys. Fluids* **25**, 095103 (2013).
  - [2] G. M. L. Good and K. P. Garry, On the use of reference models in automotive aerodynamics, in *SAE Technical Paper Series*, Technical Paper 2004-01-1308 (SAE International, 2004).
  - [3] G. Rigas, A. R. Oxlade, A. S. Morgans, and J. F. Morrison, Low-dimensional dynamics of a turbulent axisymmetric wake, *J. Fluid Mech.* **755**, R5 (2014).
  - [4] G. Pavia, M. A. Passmore, M. Varney, and G. Hodgson, Salient three-dimensional features of the turbulent wake of a simplified square-back vehicle, *J. Fluid Mech.* **888**, A33 (2020).
  - [5] G. Pavia, M. Varney, M. Passmore, and M. Almond, Three dimensional structure of the unsteady wake of an axisymmetric body, *Phys. Fluids* **31**, 025113 (2019).
  - [6] E. Berger, D. Scholz, and M. Schumm, Coherent vortex structures in the wake of a sphere and a circular disk at rest and under forced vibrations, *J. Fluids Struct.* **4**, 231 (1990).
  - [7] J. J. Miao, S. J. Wu, C. C. Hu, and J. H. Chou, Low-frequency modulations associated with vortex shedding from flow over bluff body, *AIAA J.* **42**, 1388 (2004).
  - [8] J. Yang, M. Liu, G. Wu, Q. Liu, and X. Zhang, Low-frequency characteristics in the wake of a circular disk, *Phys. Fluids* **27**, (2015).
  - [9] E. G. Duell and A. R. George, Experimental study of a ground vehicle body unsteady near wake, *SAE Technical Papers* 1999-01-0812 (SAE International, 1999).
  - [10] O. Cadot, A. Evrard, and L. Pastur, Imperfect supercritical bifurcation in a three-dimensional turbulent wake, *Phys. Rev. E* **91**, 063005 (2015).
  - [11] M. Grandemange, O. Cadot, and M. Gohlke, Reflectional symmetry breaking of the separated flow over three-dimensional bluff bodies, *Phys. Rev. E* **86**, 035302(R) (2012).
  - [12] H. Sakamoto and H. Haniu, A study on vortex shedding from spheres in a uniform flow, *J. Fluids Eng.* **112**, 386 (1990).



- [13] Y. Bury and T. Jardin, Transitions to chaos in the wake of an axisymmetric bluff body, [Phys. Lett. A \*\*376\*\*, 3219 \(2012\)](#).
- [14] A. Prasad and C. H. K. Williamson, The instability of the shear layer separating from a bluff body, [J. Fluid Mech. \*\*333\*\*, 375 \(1997\)](#).
- [15] R. Volpe, P. Devinant, and A. Kourta, Experimental characterization of the unsteady natural wake of the full-scale square back ahmed body: Flow bi-stability and spectral analysis, [Exp. Fluids \*\*56\*\*, 99 \(2015\)](#).
- [16] G. Pavia, M. Passmore, and C. Sardu, Evolution of the bi-stable wake of a square-back automotive shape, [Exp. Fluids \*\*59\*\*, 1 \(2018\)](#).
- [17] G. Bonnavion, O. Cadot, V. Herbert, S. Parpais, R. Vigneron, and J. Délery, Asymmetry and global instability of real minivans' wake, [J. Wind Eng. Ind. Aerodyn. \*\*184\*\*, 77 \(2019\)](#).
- [18] L. Dalla Longa, O. Evstafyeva, and A. S. Morgans, Simulations of the bi-modal wake past three-dimensional blunt bluff bodies, [J. Fluid Mech. \*\*866\*\*, 791 \(2019\)](#).
- [19] Y. Fan and C. Xia, Experimental and numerical analysis of the bi-stable turbulent wake of a rectangular flat-backed bluff body, [Phys. Fluids \*\*32\*\*, 105111 \(2020\)](#).
- [20] B. Podvin, S. Pellerin, Y. Fraigneau, A. Evrard, and O. Cadot, Proper orthogonal decomposition analysis and modelling of the wake deviation behind a squareback Ahmed body, [Phys. Rev. Fluids \*\*5\*\*, 064612 \(2020\)](#).
- [21] Y. Haffner, J. Borée, A. Spohn, and T. Castelain, Mechanics of bluff body drag reduction during transient near-wake reversals, [J. Fluid Mech. \*\*894\*\*, A14 \(2020\)](#).
- [22] R. D. Brackston, J. M. García de la Cruz, A. Wynn, G. Rigas, and J. F. Morrison, Stochastic modelling and feedback control of bistability in a turbulent bluff body wake, [J. Fluid Mech. \*\*802\*\*, 726 \(2016\)](#).
- [23] V. Gentile, F. F. Schrijer, B. W. Van Oudheusden, and F. Scarano, Low-frequency behavior of the turbulent axisymmetric near-wake, [Phys. Fluids \*\*28\*\*, 065102 \(2016\)](#).
- [24] G. Constantinescu and K. Squires, Numerical investigations of flow over a sphere in the subcritical and supercritical regimes, [Phys. Fluids \*\*16\*\*, 1449 \(2004\)](#).
- [25] M. Grandemange, M. Gohlke, and O. Cadot, Statistical axisymmetry of the turbulent sphere wake, [Exp. Fluids \*\*55\*\*, 1838 \(2014\)](#).
- [26] C. H. K. Williamson, Oblique and parallel modes of vortex shedding in the wake of a circular cylinder at low reynolds numbers, [J. Fluid Mech. \*\*206\*\*, 579 \(1989\)](#).
- [27] A. Prasad and C. H. K. Williamson, Three-dimensional effects in turbulent bluff body wakes, [J. Fluid Mech. \*\*343\*\*, 235 \(1997\)](#).
- [28] S. Szepessy, On the spanwise correlation of vortex shedding from a circular cylinder at high subcritical Reynolds number, [Phys. Fluids \*\*6\*\*, 2406 \(1994\)](#).
- [29] H. Eisenlohr and H. Eckelmann, Vortex splitting and its consequences in the vortex street wake of cylinders at low Reynolds number, [Phys. Fluids A \*\*1\*\*, 189 \(1989\)](#).
- [30] C. Morton and S. Yarusevych, Vortex shedding from cylinders with two step discontinuities in diameter, [J. Fluid Mech. \*\*902\*\*, A29 \(2020\)](#).
- [31] P. A. Monkewitz, A note on vortex shedding from axisymmetric bluff bodies, [J. Fluid Mech. \*\*192\*\*, 561 \(1988\)](#).
- [32] A. Evrard, O. Cadot, V. Herbert, D. Ricot, R. Vigneron, and J. Délery, Fluid force and symmetry breaking modes of a 3d bluff body with a base cavity, [J. Fluids Struct. \*\*61\*\*, 99 \(2016\)](#).
- [33] O. Evstafyeva, A. S. Morgans, and L. Dalla Longa, Simulation and feedback control of the Ahmed body flow exhibiting symmetry breaking behaviour, [J. Fluid Mech. \*\*817\*\*, R2 \(2017\)](#).
- [34] G. Rigas, A. S. Morgans, R. D. Brackston, and J. F. Morrison, Diffusive dynamics and stochastic models of turbulent axisymmetric wakes, [J. Fluid Mech. \*\*778\*\*, R2 \(2015\)](#).
- [35] A. Yakhot, H. Liu, and N. Nikitin, Turbulent flow around a wall-mounted cube: A direct numerical simulation, [Int. J. Heat Fluid Flow \*\*27\*\*, 994 \(2006\)](#).
- [36] Y. Cao and T. Tamura, Large-eddy simulation study of Reynolds number effects on the flow around a wall-mounted hemisphere in a boundary layer, [Phys. Fluids \*\*32\*\*, 025109 \(2020\)](#).
- [37] D. S. Ching and J. K. Eaton, Large-eddy simulation study of unsteady wake dynamics and geometric sensitivity on a skewed bump, [J. Fluid Mech. \*\*885\*\*, A22 \(2020\)](#).

- [38] P. Sattari, J. A. Bourgeois, and R. J. Martinuzzi, On the vortex dynamics in the wake of a finite surface-mounted square cylinder, [Exp. Fluids](#) **52**, 1149 (2012).
- [39] G. Johl, M. Passmore, and P. Render, Design methodology and performance of an indraft wind tunnel, [Aeronaut. J.](#) **108**, 465 (2004).
- [40] R. Adrian and J. Westerweel, *Particle Image Velocimetry*, Cambridge Aerospace Series (Cambridge University Press, 2011).
- [41] L. G. Göttingen, FlowMaster - Product Manual for DaVis 10.0 (LaVision GmbH, 2020).
- [42] F. Scarano and M. L. Riethmuller, Advances in iterative multigrid PIV image processing, [Exp. Fluids](#) **29**, S051 (2000).
- [43] B. Wieneke and K. Pfeiffer, Adaptive PIV with variable interrogation window size and shape (2010).
- [44] J. Westerweel and F. Scarano, Universal outlier detection for PIV data, [Exp. Fluids](#) **39**, 1096 (2005).
- [45] D. Wood, The effect of rear geometry changes on the notchback flow field, Ph.D. thesis, Loughborough University, 2015.
- [46] J. Weiss, A tutorial on the proper orthogonal decomposition, in *AIAA Aviation 2019 Forum* (American Institute of Aeronautics and Astronautics, Inc., 2019).
- [47] S. L. Brunton and J. N. Kutz, *Data-Driven Science and Engineering: Machine Learning, Dynamical Systems, and Control* (Cambridge University Press, Cambridge, 2019).
- [48] E. Varon, Y. Eulalie, S. Edwige, P. Gilotte, and J.-L. Aider, Chaotic dynamics of large-scale structures in a turbulent wake, [Phys. Rev. Fluids](#) **2**, 034604 (2017).
- [49] P. Welch, The use of fast Fourier transform for the estimation of power spectra: A method based on time averaging over short, modified periodograms, [IEEE Trans. Audio Electroacoust.](#) **15**, 70 (1967).
- [50] C. Torrence and G. P. Compo, A practical guide to wavelet analysis, [Bull. Am. Meteorol. Soc.](#) **79**, 61 (1998).
- [51] M. Kiya and Y. Abe, Turbulent elliptic wakes, [J. Fluids Struct.](#) **13**, 1041 (1999).
- [52] M. Farge, Wavelet transforms and their applications to turbulence, [Annu. Rev. Fluid Mech.](#) **24**, 395 (1992).
- [53] I. Daubechies, J. Lu, and H.-T. Wu, Synchrosqueezed wavelet transforms: An empirical mode decomposition-like tool, [Appl. Comput. Harmon. Anal.](#) **30**, 243 (2011).
- [54] S. Hoerner, *Fluid-dynamic Drag: Practical Information on Aerodynamic Drag and Hydrodynamic Resistance* (Hoerner Fluid Dynamics, Bakersfield, California, 1965).
- [55] V. Gentile, Turbulent axisymmetric base flows: Symmetry and long-term behavior, Ph.D. thesis, Delft University of Technology, 2017.
- [56] T. W. Muld, G. Efraimsson, and D. S. Henningson, Mode decomposition on surface-mounted cube, [Flow, Turbul. Combust.](#) **88**, 279 (2012).
- [57] M. Grandemange, M. Gohlke, and O. Cadot, Turbulent wake past a three-dimensional blunt body. Part 1. Global modes and bi-stability, [J. Fluid Mech.](#) **722**, 51 (2013).
- [58] F. Zhang and Y. T. Peet, Coherent motions in a turbulent wake of an axisymmetric bluff body, [J. Fluid Mech.](#) **962**, A19 (2023).
- [59] D. Burton, S. Wang, D. Tudball Smith, H. N. Scott, T. N. Crouch, and M. C. Thompson, The influence of background turbulence on ahmed-body wake bistability, [J. Fluid Mech.](#) **926**, R1 (2021).
- [60] B. Plumejeau, L. Keirsbulck, S. Delprat, M. Lippert, and W. Abassi, Behavior of the square-back ahmed body global modes at low ground clearance, [Phys. Rev. Fluids](#) **5**, 084701 (2020).
- [61] F. M. Najjar and S. Balachandar, Low-frequency unsteadiness in the wake of a normal flat plate, [J. Fluid Mech.](#) **370**, 101 (1998).
- [62] M. Lorite-Díez, J. I. Jiménez-González, L. Pastur, C. Martínez-Bazán, and O. Cadot, Experimental analysis of the effect of local base blowing on three-dimensional wake modes, [J. Fluid Mech.](#) **883**, A53 (2020).